Shap. Mem. Superelasticity (2024) 10:99–118
https://doi.org/10.1007/s40830-024-00483-z

REVIEW

Development of a Tube-Based Elastocaloric Regenerator Loaded in Compression: A Review

Stefano Dall'Olio[1] · Žiga Ahčin[1] · Andrej Žerovnik[1] · Parham Kabirifar[1,2] · Miha Brojan[1] · Jaka Tušek[1]

Received: 21 December 2023 / Revised: 13 March 2024 / Accepted: 16 March 2024 / Published online: 4 April 2024

Abstract In recent years, devices based on the elastocaloric effect (eCE) have emerged as one of the most promising alternatives to vaporcompression cooling and heating systems. After a brief overview of elastocaloric materials and elastocaloric devices developed to date, this paper reviews our recent activities in the development of tube-based elastocaloric regenerators loaded in compression. These include the evaluation of novel elastocaloric thermodynamic cycles, the characterization of the elastocaloric and fatigue behavior of Ni–Ti tubes, the thermo-hydraulic evaluation of a tube-based geometry to be applied as an elastocaloric regenerator, the buckling analysis of Ni–Ti tube in compression, and finally the development, numerical modeling, and testing of a tube-based elastocaloric regenerator in both cooling and heat-pumping modes. The developed regenerator shows a durable operation with more than 300,000 cycles, a maximum temperature span of more than 31 K at zero thermal load, and a heating power of more than 60 W at a temperature span of 10 K using only 13.7 g of elastocaloric material. In addition, further improvements of the tube-based elastocaloric regenerators related to a lower thermal mass of the regenerator's housing are shown and discussed.

Keywords Elastocaloric effect · Shape memory alloys · Buckling · Elastocaloric regenerator · Fatigue life

List of Symbols

Roman

A_f	Austenite finish temperature (K)
COP	Coefficient of performance (/)
D_{out}	Tubes outer diameter (mm)
f	Friction factor (/), frequency (Hz)
Gz	Grashof number (/)
L_g	Gauge length
NTU	Number of transfer units (/)
Nu	Nusselt number (/)
p	Pressure (Pa)
Pr	Prandtl number (/)
Re	Reynolds number (/)
t	Thickness (m)
T	Temperature (K)
V^*	Displaced fluid volume ratio (/)
Q	Heat (J)

Greek

σ	Stress (MPa)
λ	Slenderness (/)
ε	Strain (/), effectiveness (/)

Subscripts

span	Span
in	In, inner
out	Out, outer
h	Hot
c	Cold
trans	Transformation
PB	Packed bed

This invited article is part of a special topical focus in *Shape Memory and Superelasticity* on Elastocaloric Effects in Shape Memory Alloys. The issue was organized by Stefan Seelecke and Paul Motzki, Saarland University.

✉ Jaka Tušek
Jaka.Tusek@fs.uni-lj.si

[1] Faculty of Mechanical Engineering, University of Ljubljana, 1000 Ljubljana, Slovenia

[2] Department of Materials Science and Engineering, University of Maryland, College Park, MD 20742, USA

PP Parallel plates
SnT Shell-and-tube

Introduction

Cooling and air conditioning are nowadays responsible for 20% of global electricity consumption and 7.8% of all greenhouse gas emissions, but due to the rapid progress of developing countries combined with the global warming, the demand for cooling is increasing exponentially and is predicted to triple by 2050 [1]. Concurrently, heat pumps—refrigerators in heating mode—are an essential part of decarbonizing the heating sector. In 2021, about 190 million heat pump units were in operation worldwide, but they only cover 10% of global heating demand in buildings, falling short of the net-zero emission targets set for 2050. The need for alternative cooling/heat-pumping technologies has recently attracted significant attention in the scientific community since our standard cooling/heat-pumping technology, namely vapor-compression technology, uses environmentally polluting refrigerants and achieve exergy efficiencies of up to 50%, indicating that there is still room for improvement [2]. The use of conventional (synthetic) refrigerants is restricted by several climate agreements that prohibit their use in the future [3, 4]. For example, chlorofluorocarbons (CFCs), which have a high ozone depletion potential, have been phased out according to Montreal Protocol [4], while hydrofluorocarbons (HFCs), which have been used as an alternative to CFCs in recent years, have a high global warming potential and must be almost completely phased out in the next decades (according to the Kigali Amendment [3]). All synthetic refrigerants will thus need to be replaced by natural refrigerants with a lower environmental impact, such as hydrocarbons, ammonia, or CO_2. However, natural refrigerants also have their disadvantages. For example, all hydrocarbons are at least slightly flammable, ammonia is toxic, and CO_2 requires high pressure and is less efficient in hot climates [5, 6]. Therefore, it is critical to develop sustainable cooling technologies with minimal environmental impact and/or address the limitations of natural refrigerants. Over the past two decades, a great scientific effort has been devoted into developing cooling technologies based on the caloric effect of a solid refrigerant. These are potentially more efficient than vapor-compression technology and much more environmentally friendly, as they use environmentally neutral solid-state refrigerants [7]. Among the caloric technologies, elastocaloric cooling that is based on the elastocaloric effect (eCE) has been recognized as the most promising one by the US Department of Energy [8].

In this paper, we first provide a brief overview of the elastocaloric materials (eCM) and elastocaloric devices developed to date. So far, about 15 proof-of-the-concept elastocaloric devices have been presented. These devices utilize elastocaloric materials (eCMs) in different ways by applying different thermodynamic cycles, different loading modes, and different heat transfer mechanisms.

In the second part of the paper, we present an overview of our recent activities and progress in the development of the elastocaloric regenerator as a key component of the elastocaloric device. The development of an efficient, powerful and fatigue-resistant elastocaloric regenerator requires a systematic study of different interconnected aspects, such as the mechanical and elastocaloric response of eCMs [9, 10], their buckling [10, 11] and fatigue behavior [9, 10], the elastocaloric thermodynamic cycles [12], and the thermo-hydraulic properties [13] of the geometries to be applied in the elastocaloric regenerator. Due to generally better fatigue life of eCM in compression than in tension, our efforts were mainly focused on compressively loaded eCM and regenerator structures, which would assure fatigue-resistant operation. Among the geometries of eCMs available on the market, such as plates, wires and tubes, the latter have the best load-bearing capacity-to-mass ratio in compression, especially when their walls are thin, thus offering the best compromise between buckling resistance and heat transfer properties. Thin-walled structures are crucial for fast and efficient heat transfer between the eCM and the working fluid in the elastocaloric regenerator, which increases optimal operating frequency, and thus the cooling/heating power and efficiency of an elastocaloric device. The extensive research on buckling analysis of Ni–Ti tube in compression [11] and thermo-hydraulic properties od shell-and-tube geometries [7] combined with the numerical optimization of the regenerator's geometry [14, 15] led to the realization of the fatigue-resistant shell-and-tube elastocaloric regenerator. In the heat-pumping mode, the regenerator achieved a maximum temperature span of more than 31 K at zero thermal load, and a heating power of more than 60 W (equivalent to more than 4000 W/kg of eCM) at a temperature span of 10 K using only 13.7 g of eCM [16]. Figure 1 shows a roadmap of our recent research in designing regenerative elastocaloric devices and gives an overview of the challenges addressed in this paper.

In the last part of the paper, we show and discuss further improvements of the tube-based elastocaloric regenerators, focussing on the optimization of the regenerator's housing to reduce its thermal mass by using materials with low thermal conductivity to minimize the heat exchange with the surroundings. As shown in this paper, this is essential for an efficient and high-performance elastocaloric device.

Basics of the Elastocaloric Effect and Elastocaloric Materials

Shape memory materials (SMMs) are characterized by two unique properties: the shape memory effect and

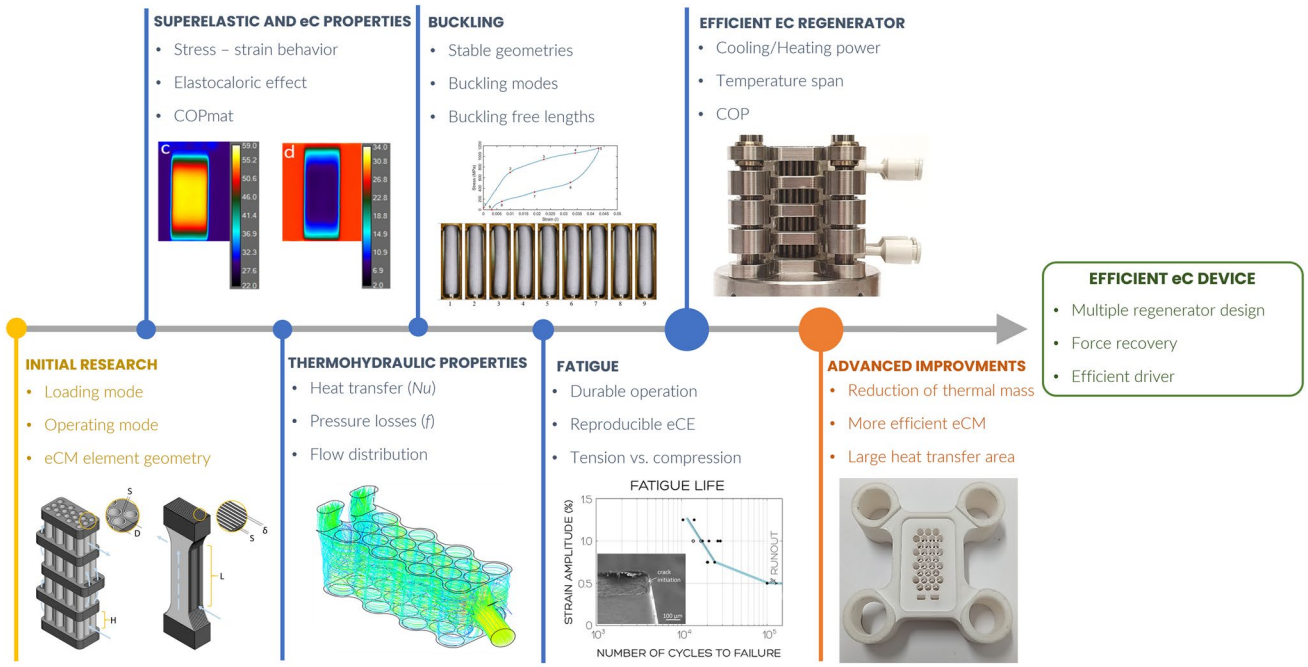

Fig. 1 Roadmap of the research in designing regenerative elastocaloric devices with an overview of the challenges addressed in this paper

superelasticity. The elastocaloric effect is closely related to superelasticity. SMMs encompass various categories, including shape memory alloys, polymers, ceramics, and gels [17]. Among these, shape memory alloys (SMAs) and shape memory polymers (SMPs) are the most commonly used and studied. While SMPs require small stresses of only up to 2 MPa but showcase significant transformation strains of up to 600%. Although some interesting demonstrators have been built using SMPs as elastocaloric materials, their overall performance is in principle poorer compared to SMAs [18–20]. This is mostly due to smaller eCE and lower thermal conductivity of SMPs, but also due to large required strains, which in the case of elastocaloric regenerator display an asymmetric fluid exchange [21]. The most studied SMA is the binary, near-equiatomic Ni–Ti alloy, which was first reported in 1963 and remains by far the most widely used SMA in various applications due to its superior fatigue behavior compared to other SMAs and its biocompatibility. As discussed in [22], other groups of SMAs include Ni–Ti-based alloys (alloyed with Cu, Co, Pd, Fe, etc.), Cu-based alloys (alloyed with Al, Ni, Zn, etc.), Fe-based alloys (alloyed with Pd, Mn, Si, Ni, etc.) and magnetic SMAs (e.g., Ni–Fe–Ga and Ni–Mn–Co), all of which are considered as potential eCMs.

Shape memory effect, superelasticity and eCE are caused by a martensitic phase transformation. This is a reversible solid-state displacive (non-diffusional) crystalline phase transformation dominated by a shear between a high-symmetry, high-temperature austenitic phase and a low-symmetry, low-temperature martensitic phase [23]. The shape memory effect enables the mechanically deformed SMA at temperatures below the martensite finish temperature (M_f) to recover ("remember") its original shape (before being deformed) when heated above the austenite finish temperature (A_f). Superelasticity enables the SMA to withstand large strains (up to 8.5%) when mechanically loaded and return to its original state after mechanical unloading above the austenite finish temperature (A_f), as shown in Fig. 2a. In both cases, the transformation is accompanied by thermodynamic irreversibility, which manifests itself as temperature and stress hysteresis. During superelastic loading and unloading, the forward martensitic transformation from austenite to martensite is exothermic and the reverse transformation is endothermic [24]. The generated heat can be dissipated under isothermal conditions, which are achieved at low strain rate, where the latent heat has simultaneously transferred to the surroundings without heating up the SMA, or, on the other hand, can heat up the sample under adiabatic conditions, which are achieved at high strain rate. The required strain rate values to achieve isothermal or adiabatic conditions depend on several factors, such as the SMA geometry and the heat transfer conditions at the surface (natural convection, forced convection, gas or liquid medium surrounding the sample) [25]. However, when the stress is removed, an endothermic transformation (martensite to austenite) occurs, cooling the sample in the case of adiabatic conditions, which can then absorb the heat from the surroundings (or a heat source). The eCE can be thus characterized as an

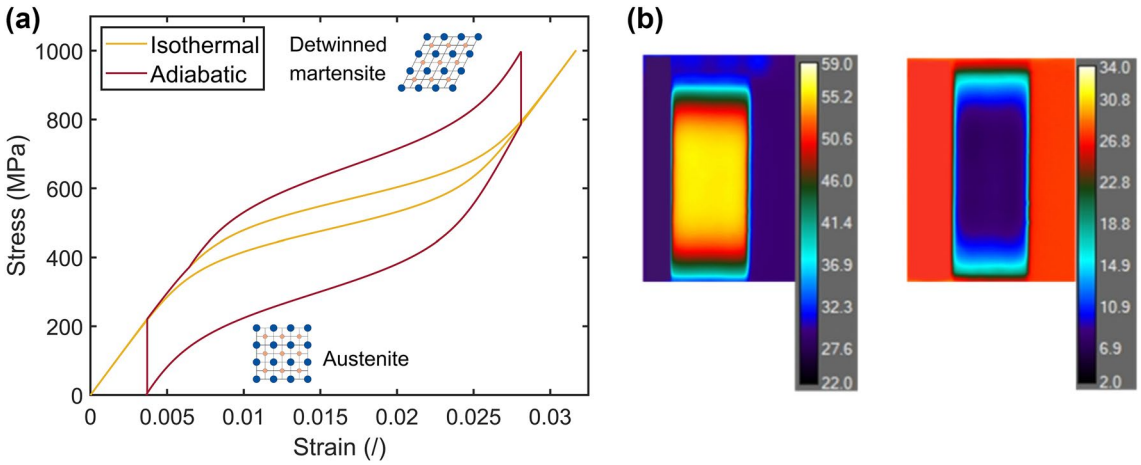

Fig. 2 Schematic representation of the superelastic response in SMA for isothermal and adiabatic conditions in the stress–strain diagram (**a**), and temperature distribution in the Ni–Ti tube after adiabatic compressive loading and unloading (note that the color bar is given in °C) (**b**) [22]

isothermal entropy change or adiabatic temperature change (see Fig. 2b).

In general, all SMAs (and shape memory polymers) can be considered as potentially eCMs if their austenitic finish temperature (A_f) is below the working temperature of the device, which is a prerequisite for reversible superelasticity. The most studied eCM is the binary Ni–Ti alloy, in which reproducible adiabatic temperature changes of up to 30 K at room temperature have been measured [12], while the latent heat of their martensitic transformation can be as high as 35 J/g [26]. Alloying binary Ni–Ti with Cu, V, and/or Co has been shown to improve fatigue life, reduce hysteresis and transformation stress, but at the expense of a lower adiabatic temperature change [27]. Similar results, with smaller hysteresis and smaller transformation stress but also smaller eCE compared to binary Ni–Ti, have also been observed in some Cu-based alloys (e.g., Cu–Al–Mn) [28] and some magnetic SMAs (e.g., Ni–Fe–Ga) [29], but most of these alloys are brittle, which is their main drawback for elastocalorics. Relatively large hysteresis and high transformation stress (especially in compression—see Fig. 3), which reduces the efficiency and increases the required input mechanical force, respectively, are the main drawbacks of binary Ni–Ti alloy. Recently, a new magnetic SMA (Ni–Mn–Ti–B) was discovered in which a reproducible adiabatic temperature change of 31.5 K was measured [30], showing that there is still room for improvement in the development of novel eCMs.

The eCM can generally be subjected to tension or compression (see Fig. 3), and each of the loading modes has certain advantages and disadvantages in terms of elastocaloric applications [22] as discussed later in the text. The most important difference between tension and compression is in fatigue life. As shown in [9], in Ni–Ti alloy fatigue-resistant operation in tension can be achieved at limited strain, and

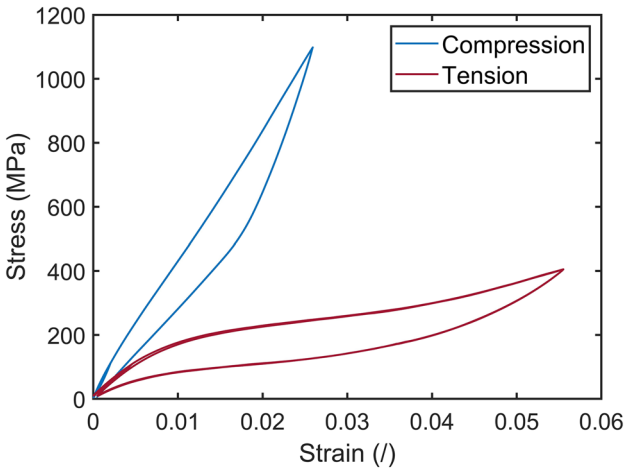

Fig. 3 Schematic representation of the tension–compression asymmetry in the case of isothermal loading of Ni–Ti alloy (tube in compression and sheet in tension) after mechanical stabilization (training)

thus limited eCE, while in compression, fatigue-resistant operation with more than 10 million cycles can be achieved at the strains corresponding to the end of the transformation plateau, and thus maximum eCE [31, 32]. However, Chluba et al. [33] demonstrated that fatigue-resistant operation can be achieved also in tension. Namely, it has been shown that thin-film Ni–Ti–Cu-based samples made by sputtering deposition that can withstand 10 million loading cycles in tension with a strain up to 2.5% and adiabatic temperature changes up to 10 K. This is strongly related to better compatibility of martensitic-austenitic interfaces compared to binary Ni–Ti [33]. It is estimated that a cooling or heat-pumping device should withstand more than 10 million loading and unloading cycles without functional and structural fatigue during its lifetime (operating 6 h per day for 10 years with operating

frequency at 1Hz)), to be used in a commercial product [34]. However, it should be noted that the superelastic response of the eCM is different in tension than in compression, which is also known as tension–compression asymmetry [35]. Kabirifar et al. [22] observed the tension–compression asymmetry in the stress–strain behavior of a superelastic Ni–Ti alloy under both isothermal (strain rate of 0.0002 s^{-1}) and adiabatic (strain rate of 0.06 s^{-1}) conditions. In compression, the slope of the transformation plateau is significantly steeper compared to tensile loading, meaning that a higher stress is required to complete the transformation, while the resulting transformation strain is smaller as shown in Fig. 3. Kabirifar et al. [22] also showed that large adiabatic temperature changes can be obtained in both compression and tension, where positive adiabatic temperature changes of up to 28 K were measured at the stress/strain levels that corresponds to the end of the transformation. Recently, Ahčin et al. [15] performed a parametric study on the fatigue-resistant parallel-plate regenerator in tension (with limited strain) and fatigue-resistant shell-and-tube regenerators in compression (made of buckling-free tubes), and showed that the shell-and-tube regenerator generates larger temperature spans due to the larger applied strain and hence a larger eCE. However, at lower temperature spans the cooling performance of the parallel-plate elastocaloric regenerator is better due to the better heat transfer geometry.

Elastocaloric Thermodynamic Cycles

As described in [36–39], the most widely applied thermodynamic cycles for utilizing caloric effect are the Otto (or Brayton) thermodynamic cycle, Stirling (or Ericsson), Carnot-like as well as a hybrid cycle (a combination of different cycles) are also possible. A typical elastocaloric thermodynamic cycle consist of loading and unloading processes and two heat transfer processes (i.e., heat absorption and heat release). In the case of Brayton and Otto cycles, the (un)loading is performed adiabatically, while in the case of Stirling and Ericsson cycle the (un)loading is performed isothermally. On the other hand, in the case of Brayton and Ericsson cycle, the heat transfer processes occur at constant stress (isostress process), while in the case of Otto and Stirling cycle, the heat transfer processes occur at constant strain (isostrain process). Since isostress processes are not easy to achieve without force sensors and complicated feedback controls [39], a great majority of thermodynamic analysis of the elastocaloric effect and devices are based on isostrain heat transfer processes (with some exceptions as discussed below), and thus on Otto thermodynamic cycle. The elastocaloric Otto cycle is based on four basic operating phases (Fig. 4). The first step is the adiabatic mechanical loading of the material (1 → 2), which causes the eCE and, thus, the temperature of the eCM increases. In the second step, heat is transferred to the surroundings at a constant (high) strain (2 → 3). The third step is the adiabatic unloading (3 → 4), where the material cools below the initial temperature. In the last step, heat is transferred from the surroundings to the eCM at a constant (low) strain (4 → 1). The entropy irreversibilities caused by hysteresis losses affect the temperature and entropy state of the eCM during loading and unloading, as shown in the temperature-entropy diagram in Fig. 4, which can significantly reduce the efficiency (coefficient of performance) of the cycle [40, 41].

The thermodynamic cycle shown in Fig. 4 (i.e., the single-stage Otto cycle) is performed in a single-stage device, where the temperature span of the device between the heat sink and the heat source is limited by the adiabatic temperature changes of the eCM. The temperature span can be increased beyond the adiabatic temperature change of the eCM by applying multi-stage thermodynamic cycles, such as cascade [42, 43], heat recovery [44, 45] and active regenerative thermodynamic cycles [16, 19, 46–49]—see section Elastocaloric devices for details. However, based on the current state-of-the-art, the active elastocaloric regenerative cycle, and thus the active elastocaloric regenerative device built around this cycle currently offers the greatest potential for practical elastocaloric applications [16, 50, 51]. If the operating conditions (frequency, mass flow rate, etc.) of a regenerative elastocaloric device are appropriate, a temperature span between the heat source temperature (T_h) and the heat sink temperature (T_c) is established in steady-state conditions. Accordingly, because of internal heat regeneration, each element of the eCM along its length performs its own thermodynamic cycle at a slightly different temperature (between T_h and T_c) as can be seen in Fig. 5a. This enables achieving larger temperature span of the device compared to the adiabatic temperature change in the eCM, which is

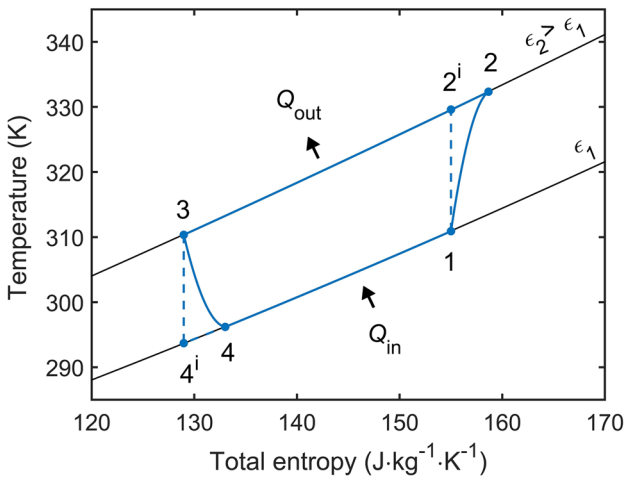

Fig. 4 Single-stage Otto thermodynamic cycle

crucial for most practical applications. However, the strong thermomechanical coupling in SMAs, as seen in Fig. 5b, results in a higher transformation stress required to initiate and complete the martensitic transformation at elevated temperatures. For practical applications where a high transformation stress is not desirable, a layered elastocaloric regenerator with different eCMs (with different transformation temperatures) has been proposed to improve the performance of elastocaloric regenerators at large temperature spans [15, 52].

While the Otto cycle is the most commonly used (elasto) caloric thermodynamic cycle, other cycles may be more efficient. In the Stirling thermodynamic cycle, mechanical loading and unloading occurs simultaneously with heat exchange with the surrounding (or heat transfer fluid) resulting in isothermal (un)loading. It should be noted that the Stirling cycle is only feasible by external or internal heat regeneration and consists of an isothermal mechanical loading of the eCM, heat regeneration at constant (high) strain, isothermal unloading of the eCM and the second heat regeneration process at constant (low) strain. The Stirling regenerative thermodynamic cycle can be more efficient because the isothermal loading reduces the required input work, but the heat transfer is less intense compared to the Otto thermodynamic cycle, resulting in a lower heating/cooling power [7]. It is important to note that isothermal loading and unloading are relatively complex processes, where the heat exchange with the HTF must be matched to the phase transformation to create isothermal conditions [7, 53].

The Carnot thermodynamic cycle has the highest theoretical efficiency, but its practical application is limited by the low cooling capacity [7]. The Carnot cycle consists of an adiabatic and isothermal mechanical loading followed by an adiabatic and isothermal mechanical unloading of the eCE. Recently, Kabirifar et al. [12] have shown that a unique Carnot-like thermodynamic cycle with improved efficiency can be generated with eCM by implementing the isostress cycle with partial transformation. As shown in Fig. 6a, at the end of the initial quasi-isothermal pre-straining (point 2) and after the first adiabatic unloading, both isostress (with constant stress during the holding period) and isostrain (with constant strain during the holding period) cycles reach the same stress–strain (also temperature) point (point 3). The difference between the isostress and isostrain cycle occurs during the holding (heat transfer) period. In an isostrain cycle, the strain is fixed, and the transformation cannot progress, therefore, only a small stress relaxation occurs (point 4^{D}). In the isostress cycle, on the other hand, the strain can freely change under the fixed stress and the transformation can continue until the actual stress–strain-ambient temperature equilibrium is reached (point 4^{F}). This is evident from Fig. 6a where the final strain of isostress cycle after the holding period (e.g., point 4^{F}) is almost identical to the strain of the quasi-isothermal pre-straining, which has occurred at the ambient temperature without self-heating/cooling effects. In contrast, the stress at point 4^{D} (end of the isostrain holding) is significantly lower than the stress of the initial quasi-isothermal pre-straining at that strain. The transformation and the heat generation/absorption continue during the holding period of an isostress cycle making it a combination of adiabatic and quasi-isothermal cycle similar to a Carnot cycle [12]. By adjusting the stress/strain range of the adiabatic part and the duration of the holding part of the cycle, the ratio between the adiabatic and quasi-isothermal parts of the cycle can be adjusted based on the heat transfer conditions to generate the optimum Carnot-like cycle for each working condition. To support and better understand the experimental results, a thermodynamic model was used to evaluate the applied elastocaloric cycles. The model is based on a phenomenological model that was used to simulate

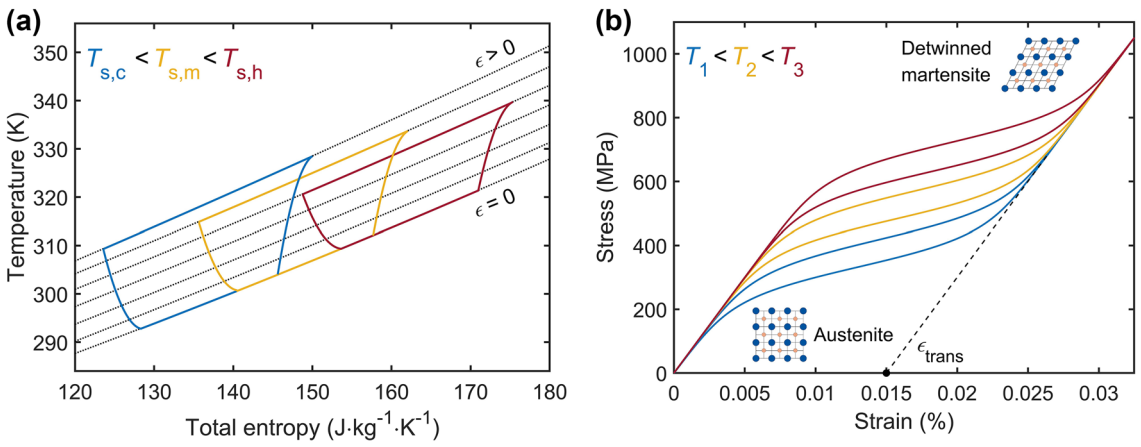

Fig. 5 Schematic representation of the active Otto thermodynamic cycle in steady state (with established temperature span) (**a**), and isothermal superelastic response in SMA for three different temperatures (**b**)

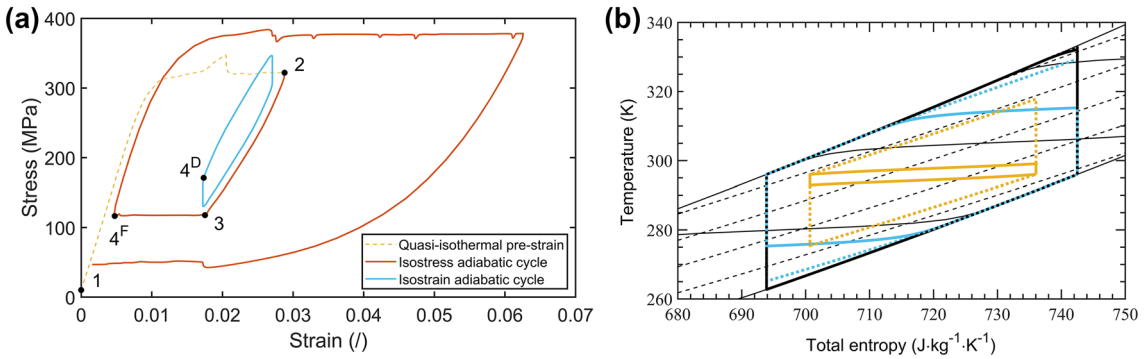

Fig. 6 Stress–strain curves (**a**) and their corresponding temperature-entropy diagrams (**b**) of an isostress (full lines) and an isostrain cycle (dashed ones) applied to Ni–Ti wires in tension

the superelastic and shape memory response of SMAs and was originally presented in [54] and in more detail in [55]. Figure 6b shows a temperature-entropy diagram of Ni–Ti wire in the case of tensile loading. An almost entirely flat stress–strain transformation plateau in tension leads to almost flat isostress lines (thin full lines in Fig. 6b) between the total entropy values at zero and at the final stress/strain points, which is due to the fact that the entire entropy change at constant stress occurs across a very narrow temperature range (almost constant temperature). Isostrain lines (thin dashed lines in Fig. 6b), on the other hand, exhibit a significantly different trend due to a nonlinear mechanical behavior, i.e., the entropy change at constant strain occurs over much wider temperature ranges for both tension and compression, as discussed in [45]. The difference between the isostress and isostrain lines in the temperature–entropy diagram opens up new avenues for manipulating the elastocaloric cooling cycle by utilizing isostress or isostrain conditions. As can be seen in Fig. 6b, the isostress cycles (thick full lines in Fig. 6b) in which most of the transformation occurs non-adiabatically during the holding period, are a good approximation of a Carnot cycle, which appears as a perfect rectangle in a temperature-entropy diagram and is theoretically the most efficient thermodynamic cycle since its input work is the minimum possible.

Elastocaloric Devices

Elastocaloric devices can be categorized according to the mechanism of heat transfer, the loading mode, and the thermodynamic operating principle (see Fig. 7). In terms of heat transfer mechanisms, we can differentiate between devices with contact heat transfer between the eCM and the heat sink/source [18, 56–58] and devices with convective heat transfer between the eCM and the heat sink/source using a heat transfer medium [42, 44–48, 53, 59, 60]. Devices with convective heat transfer, apply eCM in a macroscopically

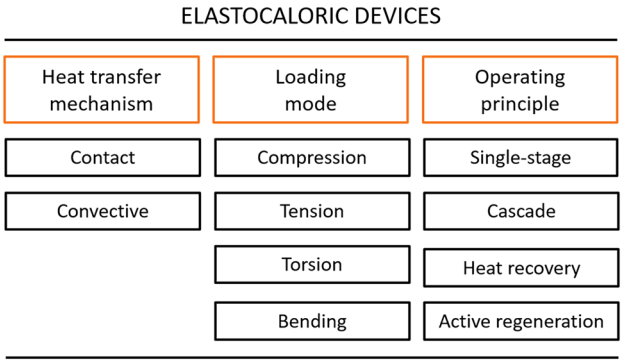

Fig. 7 Categories of elastocaloric devices based on the heat transfer mechanisms, the loading mode, and the operating principle

porous form, such as set of wires [42, 58], tubes [16, 51, 59] or parallel plates [46] through which a heat transfer fluid (air or water) can be pumped. Devices with contact heat transfer, on the other hand, usually apply a single elastocaloric element, such as sheet [56, 57, 61], membrane [18], or a set of wires [58], which oscillate between the heat sink and the heat source (or vice versa) and can be cascaded to improve the performance. Contact heat transfer devices usually apply smaller amount of eCM and are therefore limited to lower (absolute) cooling/heating powers. However, their advantage is that they can be miniaturized and potentially applied in micro-cooling applications.

Most elastocaloric devices are based on tensile [18, 42, 46, 57, 58] or compressive loading [16, 47, 48, 59, 60]. Some attempts have also been made with bending [62] and torsion/twisting [63, 64], which can reduce the required loading force (especially bending). However, these loading modes are difficult to apply in porous structures and at least some parts of the eCM in these loading modes are subjected to tension and therefore suffer from fatigue issues. Elastocaloric devices operating in tension, however, have the ability to employ thin elastocaloric elements, such as wires and sheets, that allow for rapid and efficient heat transfer

due to their thin walls, small hydraulic diameters and large heat transfer areas relative to the volume of the eCM, which should further result in high specific cooling/heating powers and high COP values. However, eCMs in tension are prone to fatigue, leading to a limited lifetime of tension-based elastocaloric devices, which is an important obstacle for practical applications. On the other hand, all compression-loaded elastocaloric devices developed to date have endured several hundred thousand load cycles, with one of them even reaching 10^7 cycles [59], without significant functional degradation or fatigue failure. The main advantage of compressive loading is therefore a significantly improved fatigue life compared to tensile loading, while its disadvantage is the buckling issue. Thin wires or sheets that would allow for rapid heat transfer cannot be compressively loaded without buckling. Designing compressive loaded elastocaloric structures with good heat transfer properties is therefore challenging because thin-walled structures, which are required for rapid heat transfer, are prone to buckling in compression. Nevertheless, three compressively loaded elastocaloric devices with record-breaking performance (outperforming even tensile-based devices) and fatigue-resistant operation have recently been developed [16, 50, 51]. They are based on a unique tube-based geometry [16, 51] or spiral-like geometry [50] with buckling-free compressive loading and relatively good heat transfer properties and have shown that it is possible to generate temperature spans of over 50 K [50], cooling/heating power of over 200 W [50, 51] and specific cooling/heating power of over 4.5 W/g of eCM [16], while maintaining fatigue-resistant operation.

As mentioned above, elastocaloric devices can be further distinguished regarding the operating principle. Single-stage devices [18, 53, 56, 63] use the simplest operating principle of elastocaloric devices, where the temperature span between the heat sink and the heat source is constrained by the adiabatic temperature change of the eCM (see Fig. 4). This limitation makes these devices unsuitable for most practical applications, given that temperature spans of about 25 K or more are normally needed. Despite this limitation, their potential is the ability for miniaturization (in combination with contact heat transfer), which makes them promising for applications in thermal management for electronic devices or chip cooling. To increase the temperature span beyond the adiabatic temperature change of the eCM, multi-stage cycles, such as heat recovery [44, 45], cascade [42, 43], and active regeneration [16, 19, 46–48] have been used. The principle of heat recovery in elastocalorics was initially introduced in [65]. Heat recovery devices comprise two or more phase-shifted elastocaloric beds (i.e., porous structures), facilitating work recovery (when one bed is compressively loaded, the other is unloaded). The process involves the mechanical loading and unloading of the beds in phase, followed by heat transfer between the cold and hot heat exchangers and the unloaded and loaded beds. Once the beds have reached the temperatures of the cold and hot heat exchangers, a heat recovery process occurs to pre-heat and pre-cool the beds prior to mechanical loading and unloading. While this increases the temperature span and can improve the efficiency of the elastocaloric device, it comes at the expense of a lower heating/cooling power due to the limited maximum operating frequency of such a concept. In a cascade configuration, multiple elastocaloric elements or beds are connected in series, with each eCM/bed operating at a different temperature, where the thermodynamic cycles are connected in series and overlap at the same time. Most of the recently developed elastocaloric devices are based on so-called active elastocaloric regenerators (AeCRs), which are porous structures made of eCM through which a heat transfer fluid (HTF) is pumped in an oscillating counter-flow direction [16, 19, 46–48]. This concept was first presented for utilizing the magnetocaloric effect in magnetic refrigeration [6]. In the active regenerative cycle, the thermodynamic cycles of each part of the eCM along the regenerator overlap in different sequences, and the heat is transferred between them by the oscillating HTF, thus carrying out the regeneration process that enables the temperature gradient along the regenerator, and thus a temperature span between the heat sink and the heat source (see Fig. 5a). Elastocaloric regenerators offer significant potential for practical applications due to their compact design and ability to achieve high temperature spans and high specific cooling/heating powers, as recently demonstrated in [16, 50, 51].

In addition to the operating principles of elastocaloric devices described above, the elastocaloric heat pipe introduces an innovative concept wherein multiple eCM beds are interconnected in series using check valves (pressure diodes) [59]. The operational principle relies on the mechanical loading and unloading of the eCM, which, driven by the eCE and related temperature changes, leads to vaporization and condensation of the HTF, altering the pressure inside the pack. As the pressure increases, the HTF is displaced into the next pack, acting as a cascade-like system. This principle offers two potential advantages over other systems: firstly, more intense heat transfer between the eCM and the HTF occurs due to evaporation and condensation can lead to higher operating frequency, and thus higher cooling/heating power, and secondly, no HTF pumping system is required, as the HTF flow is generated and regulated by pressure differences and pressure diodes between the packs.

Buckling Stability of Elastocaloric Ni–Ti Tubes

As described before, compression-based elastocaloric devices require relatively bulky elements that must withstand compressive loading without buckling in order to generate

reversible eCE. Buckling can be described as a loss of stability and collapse of the specific element. Despite the critical importance of buckling stability on designing compressive loaded elastocaloric devices, only a couple of studies focused on evaluation of buckling stability of eCM in compression [10, 11, 66, 67]. The most comprehensive study to date on buckling for the purpose of elastocaloric technology was performed by Porenta et al. [11]. They investigated the buckling responses of different Ni–Ti tubes with the objective of determining the optimal geometry of Ni–Ti tubes for elastocaloric devices. The buckling behavior of SMA tubes depends on the influencing factors such as material parameters, geometry, type of end supports, initial imperfections, etc., and need to be thoroughly investigated and well understood prior their implementation in elastocaloric devices. Porenta et al. [11] conducted a systematic investigation of the buckling stability of tubes with an approximately constant $D_{out}/t = 12$ and different D_{out} (i.e., 2 mm, 2.5 mm, and 3 mm) and tubes with constant $D_{out} = 2.5$ mm and D_{out}/t, ranging between 5 and 25. A total of 161 samples with gauge lengths between 6 and 20 mm were tested. The loading procedure included an isothermal cycle (with strain rate of 0.0003 s^{-1}) up to the stress level of 1150 MPa, which corresponds to the end of the transformation plateau. The isothermal cycle was followed by 50 training cycles (strain rate of 0.008 s^{-1}) and 20 adiabatic cycles (strain rate of 0.07 s^{-1}) as they would occur in an elastocaloric device in the case of an Otto thermodynamic cycle.

When a Ni–Ti tube is loaded in compression, the behavior of the sample can be very different and depends on the tube's geometry. Porenta et al. [11], identified various responses of thin-walled tubes in compression (see Fig. 8), and the authors divided them into three groups: stable, globally unstable, and locally unstable. Moreover, the authors further identified the following global buckling modes: global buckling (GB), buckling-unbuckling (BUB), global buckling followed by local snap through with 1 circumferential wave (GB + LB1). In the buckling–unbuckling phenomenon (BUB), the structure first starts to buckle globally during loading and then starts to straighten back even though the axial load is further increasing [68]. Although the tubes with BUB are not completely stable, they showed reversible eCE without the loss of stability and can be considered as functionally stable tubes. On the other hand, locally unstable tubes also exhibit many buckling mode shapes, of which the authors were able to categorize two specific ones, namely, local buckling (LB) with two and local buckling with more circumferential waves, as shown in Fig. 8. As mentioned in [11], the failure of the tube can occur after a few loading cycles and not necessarily only in the first cycle. One of the reasons for the failure of the tube under cyclic mechanical loading could be the accumulation of residual martensite in each cycle, known as a training effect [69]. This could affect the stress and strain distribution in the tube, causing the progressive behavior of the BUB, which means that the lateral displacements increase at each cycle and eventually lead to failure.

Porenta et al. [11] have also presented a phase diagram of buckling mode shapes for different tube dimensions and slenderness. Both diagrams in Fig. 9 show the buckling mode shapes at failure regardless of the part of the loading procedure and regardless of the number of loading cycles at which the failure has occurred. The colors of the pie charts and the numbers they contain represent the buckling mode shapes and the corresponding number of samples experiencing it. Circular pie charts indicate the absence of the BUB phenomenon in the isothermal cycle, whereas a star shape denotes the occurrence of BUB. Figure 9a gives a buckling phase diagram of the tubes with $D_{out} = 2.5$ mm but different D_{out}/t ratio, while Fig. 9b gives a buckling phase diagram of the tubes with D_{out}/t ratio of about 12 but different D_{out}. One can see from Fig. 9a that functionally stable tubes (although

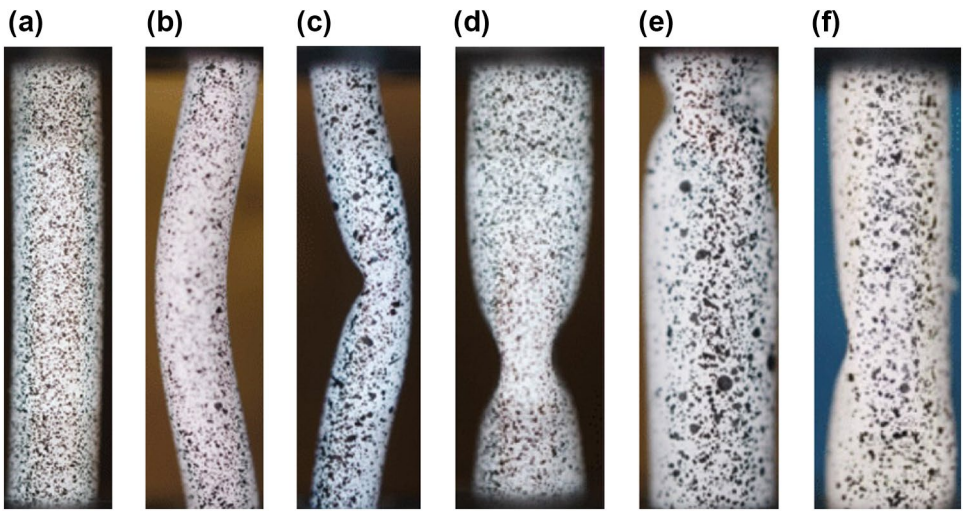

Fig. 8 Images of identified buckling modes in thin-walled Ni–Ti tubes: Buckling-unbuckling (no failure) (**a**); global buckling (**b**); global buckling + local snap-through buckling (**c**); local buckling with two circumferential waves (**d**); Local buckling with three circumferential waves (**e**); uncategorized local buckling (**f**)

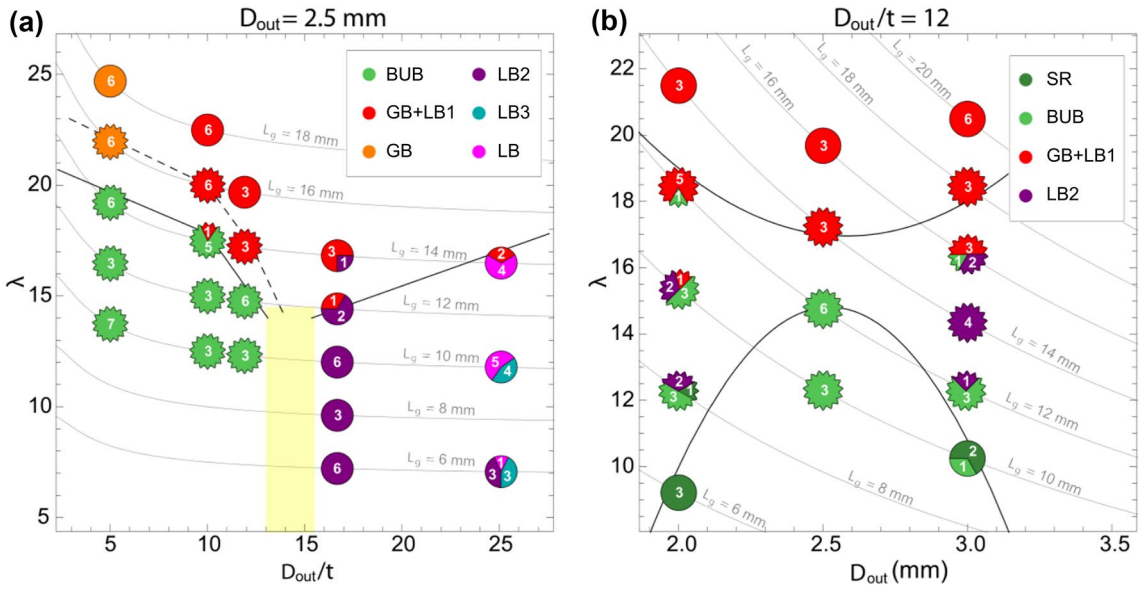

Fig. 9 Phase diagram of buckling mode shapes for the tubes of constant $D_{out}=2.5$ mm for λ—D_{out}/t space (**a**), and for the tubes of approximately constant $D_{out}/t=12$ for λ—D_{out} space (**b**)

experiencing BUB phenomena) are shorter than 14 mm and have a D_{out}/t ratio below 13, while longer tubes showed global buckling. On the other hand, all the tubes with the D_{out}/t ratio above 15 showed local buckling behavior regardless of their length. In Fig. 9b, the region of functionally stable tubes is located below the convex black curve, while above the concave black curve the GB + LB1 mode shape dominates. Between these lines, the combinations of stable, globally and locally unstable responses can be observed. The most important features in these phase diagrams are the marked regions of functionally stable tubes, which serve as a guide for future developments of elastocaloric devices and other potential applications of eCM in compression, such as dampers and actuators. Particularly for compressively loaded elastocaloric devices, it is crucial to use tubes with the longest possible length that are still functionally stable, while the wall thickness of the tube should be as thin as possible to improve the heat transfer between the eCM and the HTF. For this reason, functionally stable tubes with a higher D_{out}/t ratio are preferred.

Interestingly, as discussed in Porenta et al. [11], a large majority of the tubes that survived the training also survived the adiabatic cycling, suggesting that training alone may be an appropriate measure to determine functionally stable tubes. In addition, some tubes that exhibited BUB during the first part of the loading procedure survived the entire loading procedure. This suggests that although the tube is not completely stable, it is still functionally stable and can be potentially used in elastocaloric devices, but fatigue life of these tubes with BUB phenomena has not yet been investigated.

Thermo-Hydraulic Evaluation of Elastocaloric Regenerators

The thermo-hydraulic properties of elastocaloric porous structures (e.g., elastocaloric regenerators), such as the convective heat transfer and the pressure drop, play a decisive role in achieving good cooling or heat-pumping characteristics. Namely, an ideal elastocaloric regenerator should have a high convective heat transfer coefficient to transfer heat between the eCM and the heat transfer fluid as rapidly and efficiently as possible, but at the same time it should have low pressure drop to reduce the pumping power of the heat transfer fluid. The evaluation of thermo-hydraulic properties is therefore one of the most important steps in the development process of elastocaloric regenerators prior to their implementation in an elastocaloric device. Thermo-hydraulic correlations, such as (Nu-Re and *f*-Re) are commonly used to describe heat transfer characteristics and viscous losses in different types of heat exchangers. In general, thermo-hydraulic properties of a regenerator are evaluated using single-blow method [70], unidirectional-flow test [71], or oscillating-flow test [72]. In the last decades, several investigations of thermo-hydraulic properties of active magnetic regenerators (AMR) to be applied in magnetic refrigeration devices have been performed. One of the first works on the thermo-hydraulic properties of different regenerators to be applied as AMRs were performed by Šarlah et al. in 2012 [71]. They concluded that due to more intense heat transfer, the packed-bed AMRs can generate the highest cooling capacity and temperature span, while they show lower coefficients of performance (COP) due to

higher pressure drop compared to ordered structures, such as parallel-plate geometry. Trevizoli et al. [72] showed that oscillating-flow packed-bed regenerators can reach high thermal effectiveness (above 0.95) for NTU values above 100. The effectiveness generally increases with decreasing particle size and decreasing utilization factor.

Following the works done on thermo-hydraulic characterization of regenerators to be applied as AMRs, a similar analysis was performed for a shell-and-tube geometry proposed in [10], which has been considered as a promising structure to be applied as a compressively loaded elastocaloric regenerator. In such a configuration, baffles act as support elements that prevent buckling of the thin-walled tubes while guiding the HTF in the cross-flow over the tube bundles (on the shell side). Ahčin et al. [13] conducted a thermo-hydraulic analysis of regenerators with shell-and-tube geometry. They used an oscillating-flow experimental setup originally developed in [73], the ε-NTU method, and numerical modeling to evaluate the thermal effectiveness and develop the empirical Nu-Re and f-Re correlations for the shell side of the shell-and-tube regenerator. Nine different shell-and-tube configurations constructed from tubes with different wall thicknesses, different tube (rod) diameters, different tube (rod) spacings and different channel heights (baffle spacings) have been evaluated (see [13] for details). The design of the shell-and-tube regenerator is shown in Fig. 10.

As a result of a thermo-hydraulic analysis, new empirical correlations for the Nusselt number and the friction factor as a function of Reynolds number were developed (Fig. 11). The Nusselt number is a dimensionless parameter normally used to evaluate and compare the thermal properties of heat exchangers and regenerators. It represents the ratio of convective and conductive heat transfer in the thermal boundary layer. In general, Nu depends on flow conditions, temperature-dependent material properties and geometrical specifications. Figure 11a shows the obtained Nu-Re and f-Re correlations for the shell-and-tube geometry and their comparison with the well-established correlations of the two most widely applied geometries in caloric regenerators, namely the packed-bed [73] and parallel-plate [74] geometries. It can be seen that except for very low *Re,* the shell-and-tube geometry outperforms the parallel-plate geometry, where their Nu are much closer to the one of the packed-bed geometry.

Furthermore, the shell-side friction factor was calculated based on the pressure drop measurements across the regenerator bed [13]. Figure 11b shows a comparison of packed-bed [75] and parallel-plate [76] friction factors with the friction factor of the shell-and-tube regenerators. It can be seen that the shell-and-tube geometry has a relatively low friction factor that is more similar to the parallel-plate geometry and much smaller compared to the packed-bed geometry.

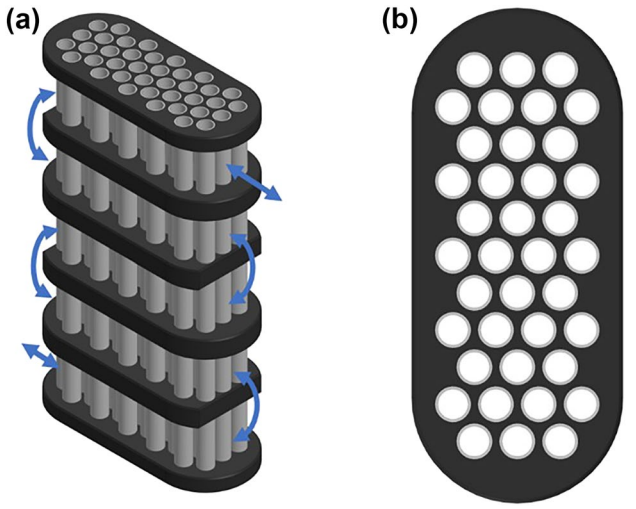

Fig. 10 The regenerator design with shell-and-tube geometry (without housing) with marked HTF flow path (**a**), and the top view of the design showing staggered tube arrangement (**b**)

Nevertheless, comparing the two thermo-hydraulic properties (Nu and f) evaluated in [13], it can be concluded that the shell-and-tube geometries represent an excellent trade-off between heat transfer and viscous losses, compared to packed-bed and parallel-plate regenerators, as the two most commonly used geometries in caloric technology. They can provide good heat transfer properties (relatively high Nu) and low pressure drop at the flow conditions relevant for ACRs ($Re < 2000$). Ahčin et al. [13] concluded that the shell-and-tube regenerator shows high potential to be applied as an elastocaloric regenerator. However, it should be noted that despite the relatively high Nu, the shell-and-tube design suffers from relatively low specific heat transfer area (note that only the outer side of the tubes are in contact with the HTF) and a relatively large hydraulic diameter, which reduces the convective heat transfer coefficient and the overall cooling/heating performance.

Development and Experimental Characterisation of Fatigue-Resistant Active Elastocaloric Regenerator

Based on fatigue and buckling stability analysis of Ni–Ti tubes [10, 11], and thermo-hydraulic evaluation of shell-and-tube geometry [13], Ahčin et al. [16] developed the elastocaloric regenerator shown in Fig. 12, which is fatigue-resistant, powerful, and relatively efficient, with an overall specific performance that surpasses most of the previously developed caloric cooling and heat-pumping devices. It consists of 18 commercial Ni–Ti tubes with an outer diameter of 3 mm and an inner diameter of 2.5 mm. The total mass of the tubes was

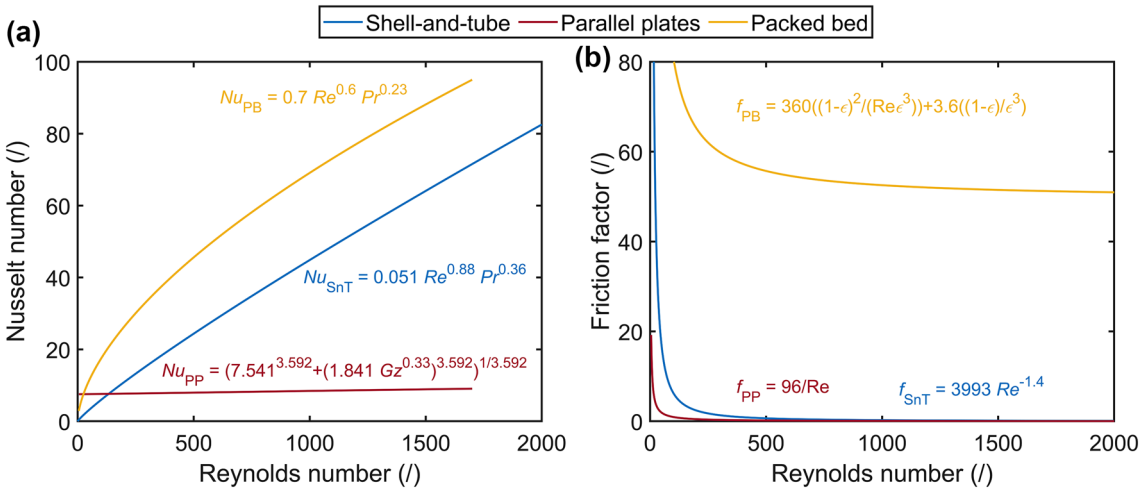

Fig. 11 Comparison of the Nu-Re (**a**), and *f-Re* empirical correlations for different regenerator geometries (**b**)

13.7 g. The tubes were cut and further polished to a length of 56.0 mm. The tubes were inserted with small clearance into five 4 mm-thick supports evenly distributed along the length of the tubes with tight fit. The gauge length (i.e., the free length between the supports) of the tubes was 9 mm. Considering more complex design of the regenerator compared to a single tube testing, the selected gauge length is slightly shorter than the stable length of this tube obtained during

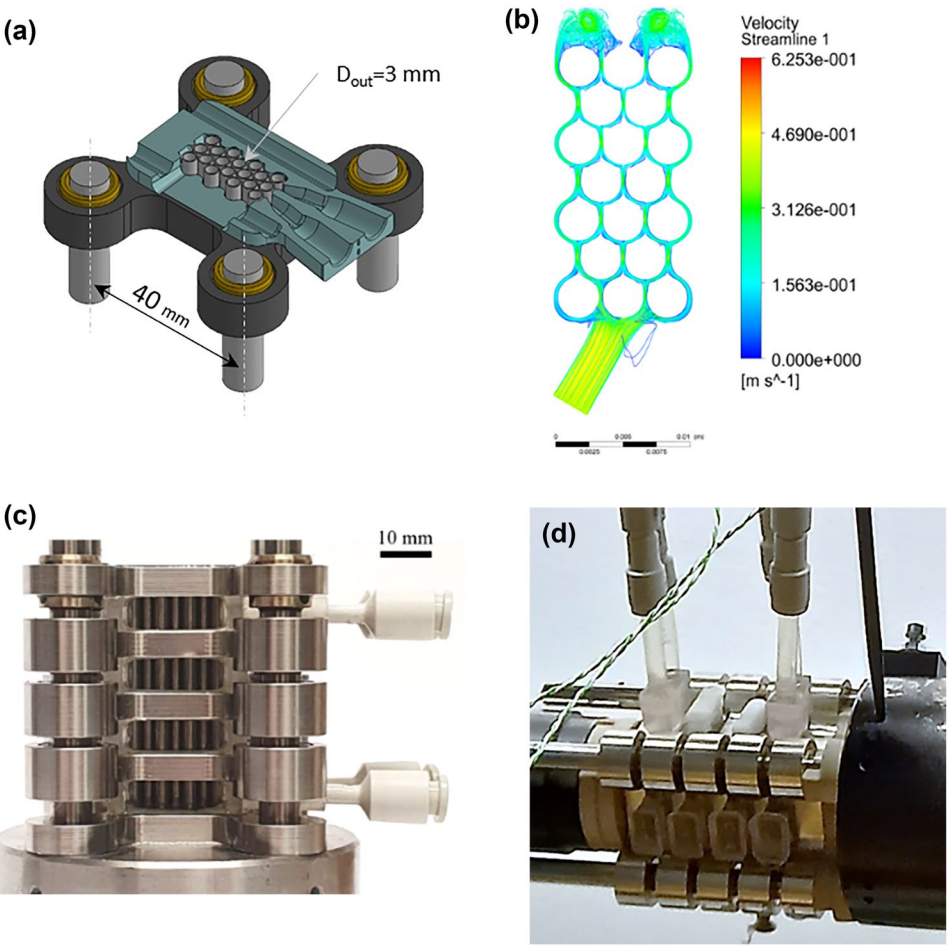

Fig. 12 CAD model of the regenerator showing a cross-section view (**a**), streamlines showing flow distribution in the first segment of the AeCR (**b**), side view of the regenerator showing the Ni–Ti tubes inside (**c**), and regenerator during tests with visible check valves (**d**)

experimental buckling analysis [11]—see Fig. 9b. The inlet geometry of the regenerator was optimized using ANSYS Fluent to allow for the optimal flow distribution between the channels (see Fig. 12a–b) and to minimize a flow maldistribution. This is crucial to achieve a uniform utilization of the eCE and efficient regeneration process and to minimize the dead volume at the inlet/outlet of the regenerator.

The first series of tests were carried out to determine the maximum temperature span without applying thermal load to the system. The tests were conducted under different operating conditions in both cooling and heat-pumping modes. Here, we report only the main results in heat-pumping mode (for more detailed results, readers should refer to [16]). Figure 13a shows an establishment of the temperature span from an initial to a steady-state operation under selected operating conditions. As can be seen, the regenerator initially reacts quickly to the applied mechanical load, especially during the first 200 s, reaching a temperature span of about 25 K. Afterwards, the temperature span increases slower, and the steady state with 31.3 K of the temperature span is reached within 1800s after the start of the experiment.

Figure 13b shows the temperature span of the AeCR as a function of the displaced volume ratio and frequency at the applied stress of 825 MPa. The displaced fluid volume ratio is defined as the ratio between the volume of HTF displaced through the regenerator in a single blow period and the volume of fluid in the regenerator. It can be seen that working at high frequency results in a higher temperature span, and the benefit of high frequency is more pronounced when operating at a low displaced volume ratio. On the contrary, at high displaced volume ratios, the effect of frequency on the temperature span is much smaller. The main reason for this behavior is that at a higher displaced volume ratio, the internal regeneration is less pronounced, and the operation of the active regenerator gravitates toward a single-stage operation, with the temperature span being equal to the adiabatic temperature change in the eCM. As a general behavior seen in the experiments, higher stress levels allow for a larger temperature span due to a larger eCE, and thus larger adiabatic temperature changes for all frequencies and displaced fluid volume ratios. It can also be seen that the temperature spans increase with increasing operating frequency for all displaced fluid volume ratios. Overall, the largest temperature spans were obtained at the highest applied frequency in this study. i.e., 2 Hz, which corresponds to a single fluid flow period of about 0.2 s (note that the loading and unloading time was set to 30 ms for all experiments).

In the second series of experiments, a thermal load was applied to the system, simulating the heating power in heat-pumping mode and the cooling power in cooling mode—see [16] for details. As the thermal load supplied to the system increases, the temperature span decreases as can be seen in Fig. 14a, which shows the temperature span evolution between fluid outlets of the regenerator in heat-pumping mode at different heating powers. As expected, the temperature span decreases with increasing the heating power. Figure 14b shows the linear dependence of the temperature span on the heating power, as normally observed in (single-layered) caloric devices [7]. The experiments were performed at an operating frequency of 2 Hz, using the same stress level (825 MPa) and different displaced fluid volume ratios. A small displaced fluid volume ratio allows for larger maximum temperature spans, but a steeper slope of the temperature span—heating power characteristics at the same stress level, and thus a lower maximum heating power (at zero temperature span) compared to a larger displaced fluid volume ratio.

Based on the heat-pumping performance, the efficiency of the regenerator was further evaluated and the results can be seen in Fig. 15a. The efficiency of a heat-pumping system is usually expressed by the COP and exergy efficiency. For the propose of this analysis we have assumed that the work released during the unloading can be fully recovered, which can be realized in an elastocaloric device including several phase-shifted elastocaloric elements/regenerators [53] and is a usual assumption when evaluating the efficiency of

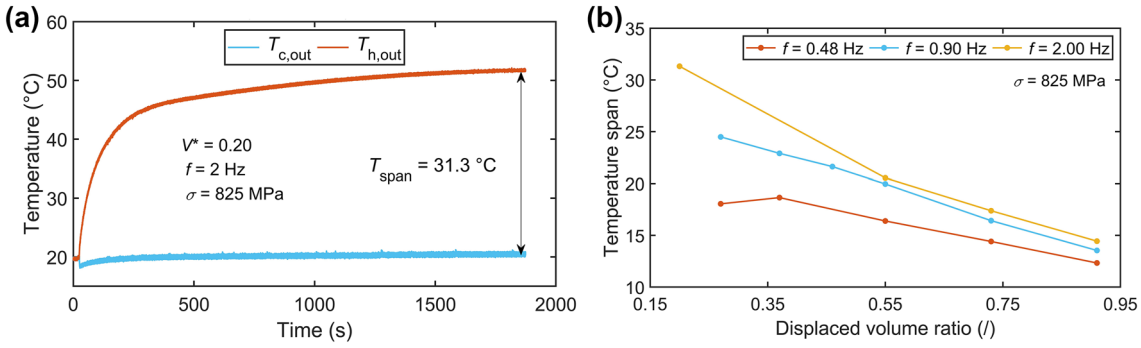

Fig. 13 Time evolution of the temperature span in the heat-pumping mode (**a**), and temperature span as a function of the displaced fluid volume ratio in the heat-pumping mode (**b**)

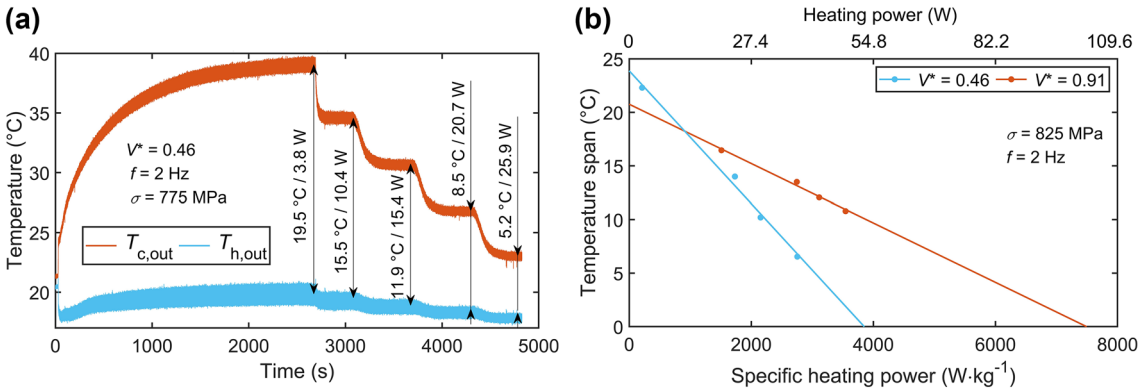

Fig. 14 Heating powers of the elastocaloric regenerator: time evolution of the temperature span due to the gradual increase of the heating power in the heat-pumping mode (**a**). Temperature span—(specific) heating power characteristics at different operating conditions (**b**)

elastocaloric devices. This means that only the hysteresis losses have been considered as mechanical input power in addition to the input power to pump the HTF. Figure 15a shows the COP values as a function of the temperature span of the regenerator under different operating conditions. For example, the COP values of 5.2 and exergy efficiencies of 11% have been obtained at a specific heating power of about 3700 W/kg (Fig. 14b) and a temperature span of about 5 K. On the other hand, at the temperature span of about 11 K and specific heating power of about 3500 W/kg, the COP of about 3.1 was obtained (corresponding to exergy efficiency of 11%).

The developed elastocaloric regenerator provided one of the best functionally stable overall performance among the elastocaloric devices developed to date. It demonstrated fatigue-resistant operation with more than 300,000 loading cycles at stress levels of up to 825 MPa (see Fig. 15b) with no signs of performance degradation when operating in cooling or heat-pumping mode over a wide temperature range. Figure 15b shows the selected stress–strain curves of the regenerator at different number of performed cycles and different stress levels.

A direct comparison of the different elastocaloric devices in terms of the maximum temperature span and the maximum specific cooling/heating power of the devices is given in Fig. 16. It should be noted that the maximum temperature span and the maximum specific cooling/heating power are not achieved simultaneously (i.e., at the same operating conditions). As normally observed in caloric devices [7], the maximum temperature span is achieved at the smallest/zero cooling/heating power, while the maximum specific cooling power is achieved at the smallest/zero temperature span.

Improving Regenerator Performance: Thermal Mass Reduction

With the aim of improving the performance of the shell-and-tube elastocaloric regenerator, we have recently studied the impact of the support elements (baffles) and their thermal mass on the performance of the AeCR. We have therefore investigated different configurations and materials of the supports (see Fig. 17) to improve the performance of the elastocaloric regenerator. These were steel supports

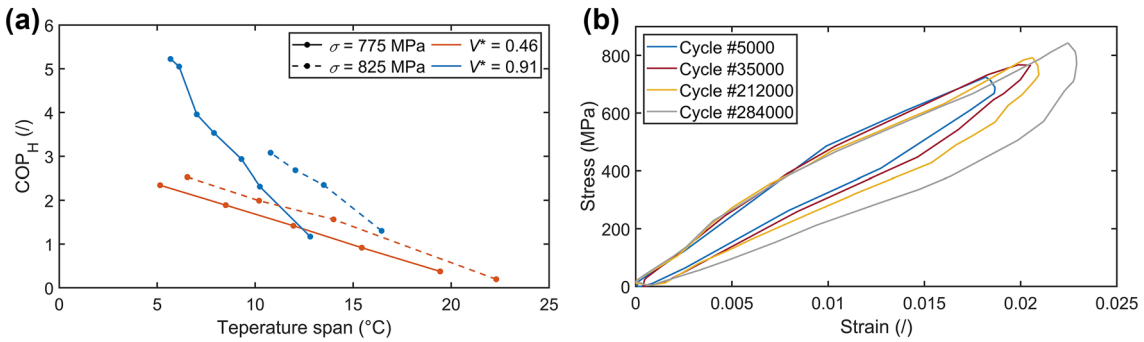

Fig. 15 Heating COP values as a function of the temperature span (**a**), and stress–strain curve as a function of the number of cycles performed by the regenerator (**b**)

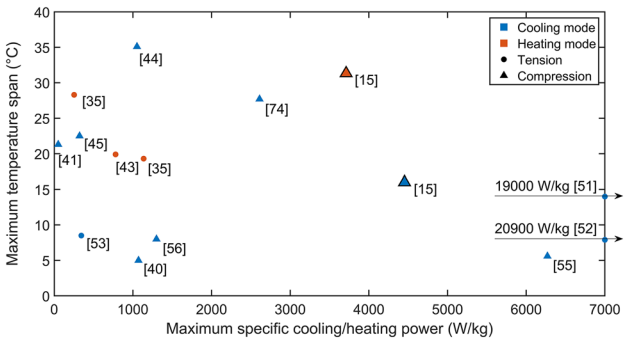

Fig. 16 A comparison of the maximum temperature span and the maximum specific cooling/heating power of the best elastocaloric cooling and heat-pump devices developed to date [77]

(Fig. 17a), steel supports laminated with PEEK insulation (Fig. 17b), and 3D-printed supports made of Rigid 10K resin (Fig. 17c) with a tensile modulus of 11 GPa and a flexural strength of about 160 MPa.

The regenerators with steel supports and steel supports laminated with PEEK insulation were essentially equal (with the tubes with an outer diameter of 3 mm, an inner diameter of 2.5 mm with the total length of 56 mm in four stages). The regenerator with 3D-printed supports had only two stages with 31 Ni–Ti tubes with an outer diameter of 2.5 mm, an inner diameter of 2.0 mm, and a length of 34 mm (see Fig. 18) as it was only intended to test the suitability of Rigid 10K 3D printed supports for this type of elastocaloric regenerator. The initial experimental results with 3D printed supports were promising, as it achieved a maximum temperature span of 19.8 K at a stress of 750 MPa, with a V^* of 0.26 and at a frequency of 1 Hz. However, the regenerator showed poor fatigue performance, as the supports cracked in a vicinity of the tubes after about 50,000 cycles (at the stress levels in a range between 750 and 800 MPa), causing the tubes to buckle, and thus fail. Namely, the outer diameter of the tube is increased upon loading, causing increased stress on the supports. Therefore, further investigation of low thermal conductivity support materials with increased stiffness and reduced brittleness needs to be carried out.

To understand the effect of the thermal mass of the supports we investigated the effects of different support configurations on the performance of the shell-and-tube elastocaloric using a numerical model and the method presented in [14, 15]. We have studied the regenerator's performance made of steel supports laminated with PEEK insulation (see Fig. 17) and Rigid 10K 3D printed supports (see Fig. 18). In both cases a temperature span of 15 K with a cold-side temperature of 288 K and a hot-side temperature of 303 K was prescribed and the effects of tube diameter and tube wall thickness on the cooling performance at different operating conditions were investigated. The spacing between the tubes was set to 0.3 mm and the spacing between the baffles to 8 mm. The geometry of the regenerator was limited by the use of mechanically stable tubes that can withstand a compression at 1000 MPa according to Porenta et al. [11] and the total length of the tubes was set to 100 mm. Figure 19 shows the cooling power and COP of the shell-and-tube elastocaloric regenerator with steel supports laminated with PEEK insulation. It can be seen that the optimum wall thickness depends on the tube diameter and the operating conditions. Overall, the best cooling performance of the elastocaloric regenerator is achieved with tubes with an outer diameter of 2 mm and a wall thickness of 0.75 mm, which achieve a maximum specific cooling power of 1850 W/kg of eCM, and a maximum COP of 0.64 at a temperature span of 15 K.

Figure 20 shows the performance of the shell-and-tube elastocaloric regenerator with 3D-printed supports made of Rigid 10K resin under the same operating conditions and geometric constraints as the elastocaloric regenerator with steel supports laminated with PEEK insulation. Remarkably, a significant improvement in regenerator's performance can be observed. The highest specific cooling

Fig. 17 Three different support configurations tested: steel supports (**a**), steel supports with PEEK insulation (**b**), and 3D-printed supports (**c**)

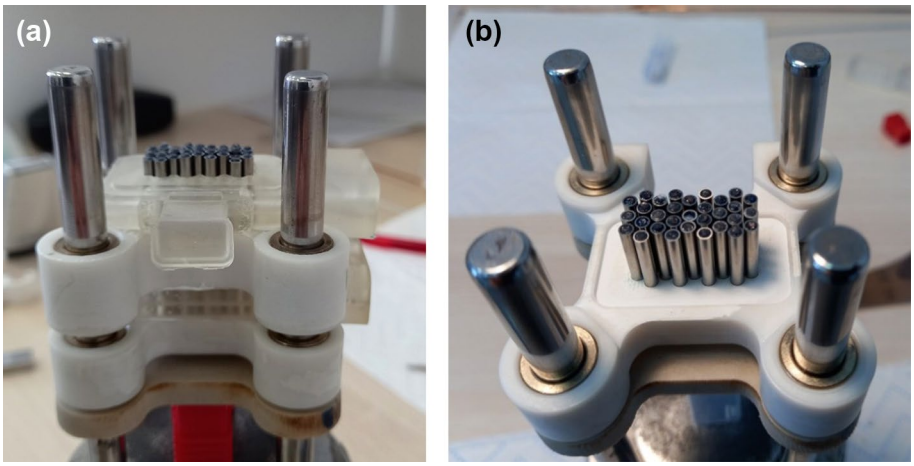

Fig. 18 Regenerator with Rigid 10K 3D printed supports. Side view of the regenerator (**a**), and a view of the regenerator without the housing (**b**)

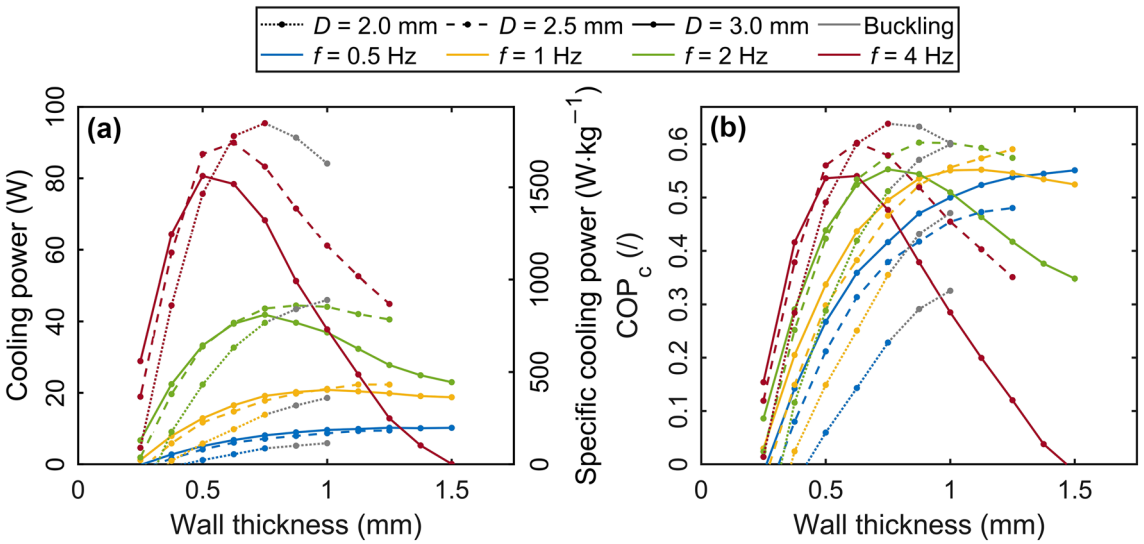

Fig. 19 Cooling power (**a**) and COP (**b**) of the shell-and-tube elastocaloric regenerator with steel supports laminated with PEEK insulation at 15 K of temperature span as a function of the wall thickness of the tubes with different outer diameters and different frequencies [15]

power of 5180 W/kg is achieved with tubes with an outer diameter of 2 mm and a wall thickness of 0.5 mm and a corresponding COP of about 1.7. On the other hand, the most efficient geometry (with the highest COP) is achieved with tubes with an outer diameter of 2 mm and a wall thickness of 0.75 mm, whereby a COP of about 1.9 can be achieved. These results demonstrate the potential advances in geometry design and performance gains associated with the implementation of low-thermal conductivity 3D-printed supports and demonstrate a promising direction for improving the overall performance of elastocaloric devices. Moreover, one can see that the support material and its thermal mass significantly influence the optimal wall thickness of the tubes, since the regenerator with steel supports requires thicker walls compared the regenerator with 3D-printed plastic supports due to the parasitic losses caused by the heat exchange between the tubes and the supports.

Conclusions

This paper provides a comprehensive overview of the research behind the development of the shell-and-tube elastocaloric regenerator. Our research covers several critical aspects, starting with the selection of suitable eCM. We have investigated the buckling stability of potential elastocaloric tubes, and performed systematic evaluation of the thermo-hydraulic properties of geometries that seem promising for elastocaloric applications (i.e., shell-and-tube design). The ultimate goal of this research was to develop an elastocaloric regenerator that provides durable and fatigue-resistant

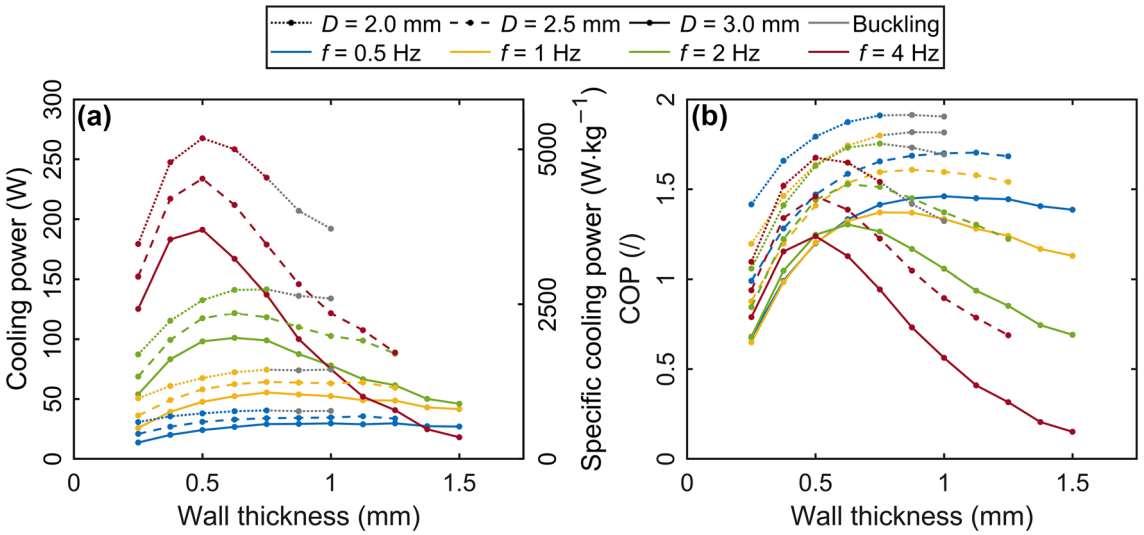

Fig. 20 Cooling power (**a**) and COP (**b**) of the shell-and-tube elastocaloric regenerator with 3D-printed supports made of Rigid 10K resin at 15 K of temperature span as a function of the wall thickness of the tubes with different outer diameters and different frequencies

operation while ensuring efficient heat transfer and low pressure drop.

The resulting regenerator provided one of the best overall performances among the elastocaloric devices developed to date. It has demonstrated fatigue-resistant operation, enduring over 300,000 loading cycles at stress levels of up to 825 MPa with no signs of performance degradation. Operating in both cooling and heat-pumping modes across a broad temperature range, the regenerator achieved a COP value of up to 5.2 at a specific heating power of about 3700 W/kg and a temperature span of about 5 K.

Further improvements of the shell-and-tube elastocaloric regenerator are possible. The future focus should be on elastocaloric materials with smaller hysteresis and transformation stresses as well as on an improved regenerator geometry with larger heat transfer area per mass of eCM and optimization of the supporting structure in terms of minimizing its thermal mass. Our research showcases the viability of constructing a regenerator with polymer supports, which according to numerical investigation provides a significant increase in regenerator performance. However, further investigation of potential materials for the supports needs to be carried out to improve the fatigue life of the regenerator with polymer supports.

Highly motivated by the excellent results achieved with a single elastocaloric regenerator, our ongoing efforts are directed toward the development of a preindustrial, multi-regenerator elastocaloric device. This advanced design features four phase-shifted regenerators with integrated work recovery mechanism, aiming to increase the efficiency and cooling/heating power compared to a single regenerator. Finally, the overarching goal is to achieve cooling/heating performance comparable to that of a small-scale vapor-compression device, thereby advancing the applicability and efficiency of elastocaloric technology in cooling and heating applications.

Acknowledgements This work was supported by the European Research Council under the Horizon 2020 program (ERC starting grant no. 803669). The authors would also like to acknowledge the support of the Slovenian Research Agency (Core funding no. P2-0422).

Data Availability The datasets presented in this study are available from the corresponding author upon reasonable request.

References

1. Coulomb D, Dupont J-L, Marlet V (2017) 35th Informatory note on refrigeration technologies. The impact of the refrigeration sector on climate change, France
2. Schipper J, Bach D, Mönch S, Molin C, Gebhardt S, Wöllenstein J, Schäfer-Welsen O, Vogel C, Langebach R, Bartholomé K (2023) On the efficiency of caloric materials in direct comparison with

exergetic grades of compressors. J Phys Energy 5:45002. https://doi.org/10.1088/2515-7655/ace7f4
3. Kigali Amendment to the Montreal Protocol: A crucial Step in the Fight Against Catastrophic Climate Change, Environmental investigation agency (2016)
4. Ozone Secretariat. Handbook for the Montreal protocol on substances that deplete the ozone layer (2020)
5. Kauffeld M (2016) 31st Informatory note on refrigeration technologies. Current long-term alternative refrigerants and their applications
6. IEA (n.d.) Average efficiency of new air conditioners 2000–2020 and in the Net Zero Scenario, Paris. https://www.iea.org/data-and-statistics/charts/average-efficiency-of-new-air-conditioners-2000-2020-and-in-the-net-zero-scenario
7. Kitanovski A, Tušek J, Tomc U, Plaznik U, Ožbolt M, Poredoš A (2015) Magnetocaloric energy conversion—from theory to applications. Springer, Berlin
8. Goetzler W, Zogg R, Young J, Johnson C (2014) Energy savings potential and RD & D opportunities for non-vapor-compression HVAC technologies, US Dep. Energy, p 3673. https://doi.org/10.2172/1220817
9. Tušek J, Žerovnik A, Čebron M, Brojan M, Žužek B, Engelbrecht K, Cadelli A (2018) Elastocaloric effect vs fatigue life: exploring the durability limits of Ni-Ti plates under pre-strain conditions for elastocaloric cooling. Acta Mater 150:295–307. https://doi.org/10.1016/j.actamat.2018.03.032
10. Porenta L, Kabirifar P, Žerovnik A, Čebron M, Žužek B, Dolenec M, Brojan M, Tušek J (2020) Thin-walled Ni-Ti tubes under compression: ideal candidates for efficient and fatigue-resistant elastocaloric cooling. Appl Mater Today 20:100712. https://doi.org/10.1016/j.apmt.2020.100712
11. Porenta L, Trojer J, Brojan M, Tušek J (2022) Experimental investigation of buckling stability of superelastic Ni-Ti tubes under cyclic compressive loading: towards defining functionally stable tubes for elastocaloric cooling. Int J Solids Struct 256:111948. https://doi.org/10.1016/j.ijsolstr.2022.111948
12. Kabirifar P, Trojer J, Brojan M, Tušek J (2022) From the elastocaloric effect towards an efficient thermodynamic cycle. J Phys Energy 4:44009. https://doi.org/10.1088/2515-7655/ac92a5
13. Ahčin Ž, Liang J, Engelbrecht K, Tušek J (2021) Thermo-hydraulic evaluation of oscillating-flow shell-and-tube-like regenerators for (elasto)caloric cooling. Appl Therm Eng 190:116842. https://doi.org/10.1016/j.applthermaleng.2021.116842
14. Ahčin Ž, Kabirifar P, Porenta L, Brojan M, Tušek J (2022) Numerical modeling of shell-and-tube-like elastocaloric regenerator. Energies. https://doi.org/10.3390/en15239253
15. Ahčin Ž, Tušek J (2023) Parametric analysis of fatigue-resistant elastocaloric regenerators: tensile vs compressive loading. Appl Therm Eng. https://doi.org/10.1016/j.applthermaleng.2023.120996
16. Ahčin Ž, Dall'Olio S, Žerovnik A, Baškovič UŽ, Porenta L, Kabirifar P, Cerar J, Zupan S, Brojan M, Klemenc J, Tušek J (2022) High-performance cooling and heat pumping based on fatigue-resistant elastocaloric effect in compression. Joule 6:2338–2357. https://doi.org/10.1016/j.joule.2022.08.011
17. Sun LY, Huang WM, Ding Z, Zhao Y, Wang CC, Purnawali H, Tang C (2012) Stimulus-responsive shape memory materials: a review. Mater Des 33:577–640
18. Greibich F, Schwödiauer R, Mao G, Wirthl D, Drack M, Baumgartner R, Kogler A, Stadlbauer J, Bauer S, Arnold N, Kaltenbrunner M (2021) Elastocaloric heat pump with specific cooling power of 20.9 W g–1 exploiting snap-through instability and strain-induced crystallization. Nat Energy 6:260–267. https://doi.org/10.1038/s41560-020-00770-w
19. Sebald G, Lombardi G, Coativy G, Jay J, Lebrun L, Komiya A (2023) High-performance polymer-based regenerative elastocaloric cooler. Appl Therm Eng 223:120016. https://doi.org/10.1016/j.applthermaleng.2023.120016
20. Ludwig C, Leutner J, Prucker O, Rühe J, Kohl M (2024) Miniature-scale elastocaloric cooling by rubber-based foils. J Phys Energy 6:15009. https://doi.org/10.1088/2515-7655/ad0cff
21. Wang K, Overvelde JTB, Engelbrecht K, Bjørk R, Bahl CRH (2023) Volume compensation of large-deformation 3D-printed soft elastomeric elastocaloric regenerators. Appl Phys Lett 123:223904. https://doi.org/10.1063/5.0177761
22. Kabirifar P, Žerovnik A, Ahčin Ž, Porenta L, Brojan M, Tušek J (2019) Elastocaloric cooling: state-of-the-art and future challenges in designing regenerative elastocaloric devices. Stroj Vestnik/J Mech Eng. https://doi.org/10.5545/sv-jme.2019.6369
23. Lagoudas DC (2008) Shape memory alloys. Springer, Boston. https://doi.org/10.1007/978-0-387-47685-8
24. Michaelis N, Schütze A, Welsch F, Kirsch S-M, Seelecke S (2019) Novel experimental approach to determine elastocaloric latent heat. Shape Mem Superelast 5:352–361. https://doi.org/10.1007/s40830-019-00249-y
25. Cheng S (2023) Comprehensive characterization of the adiabatic temperature change and (convection) heat transfer coefficient of a NiTi tube elastocaloric refrigerant. AIP Adv 13:65202. https://doi.org/10.1063/5.0147729
26. Wu Y, Ertekin E, Sehitoglu H (2017) Elastocaloric cooling capacity of shape memory alloys—role of deformation temperatures, mechanical cycling, stress hysteresis and inhomogeneity of transformation. Acta Mater 135:158–176. https://doi.org/10.1016/j.actamat.2017.06.012
27. Schmidt M, Ullrich J, Wieczorek A, Frenzel J, Schütze A, Eggeler G, Seelecke S (2015) Thermal stabilization of NiTiCuV shape memory alloys: observations during elastocaloric training. Shape Mem Superelast 1:132–141. https://doi.org/10.1007/s40830-015-0021-4
28. Xu S, Huang H-Y, Xie J, Takekawa S, Xu X, Omori T, Kainuma R (2016) Giant elastocaloric effect covering wide temperature range in columnar-grained Cu71.5Al17.5Mn11 shape memory alloy. APL Mater 4:106106. https://doi.org/10.1063/1.4964621
29. Huang X-M, Zhao Y, Yan H-L, Jia N, Yang B, Li Z, Zhang Y, Esling C, Zhao X, Ren Q, Tong X, Zuo L (2023) Enhanced cyclic stability and enlarged working temperature window of NiFeGa elastocaloric refrigerant via introducing strong texture and ductile interfacial precipitate. Scr Mater 234:115544. https://doi.org/10.1016/j.scriptamat.2023.115544
30. Cong D, Xiong W, Planes A, Ren Y, Mañosa L, Cao P, Nie Z, Sun X, Yang Z, Hong X, Wang Y (2019) Colossal elastocaloric effect in ferroelastic Ni-Mn-Ti alloys. Phys Rev Lett 122:255703. https://doi.org/10.1103/PhysRevLett.122.255703
31. Liang D, Wang Q, Chu K, Chen J, Hua P, Ren F, Sun Q (2022) Ultrahigh cycle fatigue of nanocrystalline NiTi tubes for elastocaloric cooling. Appl Mater Today 26:101377. https://doi.org/10.1016/j.apmt.2022.101377
32. Chen J, Zhang K, Kan Q, Yin H, Sun Q (2019) Ultra-high fatigue life of NiTi cylinders for compression-based elastocaloric cooling. Appl Phys Lett 115:93902. https://doi.org/10.1063/1.5115793
33. Chluba C, Ge W, de Miranda RL, Strobel J, Kienle L, Quandt E, Wuttig M (2015) Ultralow-fatigue shape memory alloy films. Science 348:1004–1007. https://doi.org/10.1126/science.1261164
34. Cui J, Wu Y, Muehlbauer J, Hwang Y, Radermacher R, Fackler S, Wuttig M, Takeuchi I (2012) Demonstration of high efficiency elastocaloric cooling with large ΔT using NiTi wires. Appl Phys Lett 101:73904. https://doi.org/10.1063/1.4746257
35. Gall K, Sehitoglu H, Chumlyakov YI, Kireeva IV (1999) Tension–compression asymmetry of the stress–strain response in aged

single crystal and polycrystalline NiTi. Acta Mater 47:1203–1217. https://doi.org/10.1016/S1359-6454(98)00432-7
36. Kitanovski A, Plaznik U, Tušek J, Poredoš A (2014) New thermodynamic cycles for magnetic refrigeration. Int J Refrig 37:28–35. https://doi.org/10.1016/j.ijrefrig.2013.05.014
37. Plaznik U, Tušek J, Kitanovski A, Poredoš A (2013) Numerical and experimental analyses of different magnetic thermodynamic cycles with an active magnetic regenerator. Appl Therm Eng 59:52–59. https://doi.org/10.1016/j.applthermaleng.2013.05.019
38. Qian S, Geng Y, Wang Y, Ling J, Hwang Y, Radermacher R, Takeuchi I, Cui J (2016) A review of elastocaloric cooling: materials, cycles and system integrations. Int J Refrig 64:1–19. https://doi.org/10.1016/j.ijrefrig.2015.12.001
39. Qian S (2023) Thermodynamics of elastocaloric cooling and heat pump cycles. Appl Therm Eng 219:119540. https://doi.org/10.1016/j.applthermaleng.2022.119540
40. Masche M, Ianniciello L, Tušek J, Engelbrecht K (2021) Impact of hysteresis on caloric cooling performance. Int J Refrig 121:302–312. https://doi.org/10.1016/j.ijrefrig.2020.10.012
41. Hess T, Maier LM, Bachmann N, Corhan P, Schäfer-Welsen O, Wöllenstein J, Bartholomé K (2020) Thermal hysteresis and its impact on the efficiency of first-order caloric materials. J Appl Phys 127:75103. https://doi.org/10.1063/1.5132897
42. Snodgrass R, Erickson D (2019) A multistage elastocaloric refrigerator and heat pump with 28 K temperature span. Sci Rep 9:1–10. https://doi.org/10.1038/s41598-019-54411-8
43. Ulpiani G, Bruederlin F, Weidemann R, Ranzi G, Santamouris M, Kohl M (2020) Upscaling of SMA film-based elastocaloric cooling. Appl Therm Eng 180:115867. https://doi.org/10.1016/j.applthermaleng.2020.115867
44. Qian S, Geng Y, Wang Y, Muehlbauer J, Ling J, Hwang Y, Radermacher R, Takeuchi I (2016) Design of a hydraulically driven compressive elastocaloric cooling system. Sci Technol Built Environ 22:500–506. https://doi.org/10.1080/23744731.2016.1171630
45. Qian S, Wu Y, Ling J, Muehlbauer J, Hwang Y, Takeuchi I, Radermacher R (2015) Design, development and testing of a compressive thermoelastic cooling prototype. Int Congress Refrig
46. Tušek J, Engelbrecht K, Eriksen D, Dall'Olio S, Tušek J, Pryds N (2016) A regenerative elastocaloric heat pump. Nat Energy 1:16134. https://doi.org/10.1038/nenergy.2016.134
47. Ianniciello L, Bartholomé K, Fitger A, Engelbrecht K (2022) Long life elastocaloric regenerator operating under compression. Appl Therm Eng 202:117838. https://doi.org/10.1016/j.applthermaleng.2021.117838
48. Catalini D (2021) Development of cooling systems with active elastocaloric regenerators. Univeristy of Maryland
49. Engelbrecht K, Tušek J, Eriksen D, Lei T, Lee CY, Tušek J, Pryds N (2017) A regenerative elastocaloric device: experimental results. J Phys D Appl Phys. https://doi.org/10.1088/1361-6463/aa8656
50. Zhou G, Zhu Y, Yao S, Sun Q (2023) Giant temperature span and cooling power in elastocaloric regenerator. Joule. https://doi.org/10.1016/j.joule.2023.07.004
51. Qian S, Catalini D, Muehlbauer J, Liu B, Mevada H, Hou H, Hwang Y, Radermacher R, Takeuchi I (2023) High-performance multimode elastocaloric cooling system. Science 380:722–727. https://doi.org/10.1126/science.adg7043
52. Engelbrecht K (2019) Future prospects for elastocaloric devices. J Phys Energy 1:21001. https://doi.org/10.1088/2515-7655/ab1573
53. Kirsch S-M, Welsch F, Michaelis N, Schmidt M, Wieczorek A, Frenzel J, Eggeler G, Schütze A, Seelecke S (2018) NiTi-based elastocaloric cooling on the macroscale: from basic concepts to realization. Energy Technol 6:1567–1587. https://doi.org/10.1002/ente.201800152
54. Tušek J, Engelbrecht K, Millán-Solsona R, Mañosa L, Vives E, Mikkelsen LP, Pryds N (2015) The elastocaloric effect: a way to cool efficiently. Adv Energy Mater 5:1500361. https://doi.org/10.1002/aenm.201500361
55. Tušek J, Engelbrecht K, Mañosa L, Vives E, Pryds N (2016) Understanding the thermodynamic properties of the elastocaloric effect through experimentation and modelling. Shape Mem Superelast 2:317–329. https://doi.org/10.1007/s40830-016-0094-8
56. Schmidt M, Schütze A, Seelecke S (2015) Scientific test setup for investigation of shape memory alloy based elastocaloric cooling processes. Int J Refrig 54:88–97. https://doi.org/10.1016/j.ijrefrig.2015.03.001
57. Bruederlin F, Bumke L, Chluba C, Ossmer H, Quandt E, Kohl M (2018) Elastocaloric cooling on the miniature scale: a review on materials and device engineering. Energy Technol 6:1588–1604. https://doi.org/10.1002/ente.201800137
58. Chen Y, Wang Y, Sun W, Qian S, Liu J (2022) A compact elastocaloric refrigerator. Innovation 3:100205. https://doi.org/10.1016/j.xinn.2022.100205
59. Bachmann N, Fitger A, Maier LM, Mahlke A, Schäfer-Welsen O, Koch T, Bartholomé K (2021) Long-term stable compressive elastocaloric cooling system with latent heat transfer. Commun Phys. https://doi.org/10.1038/s42005-021-00697-y
60. Zhang J, Zhu Y, Cheng S, Yao S, Sun Q (2022) Enhancing cooling performance of NiTi elastocaloric tube refrigerant via internal grooving. Appl Therm Eng. https://doi.org/10.1016/j.applthermaleng.2022.118657
61. Bruederlin F, Bumke L, Quandt E, Kohl M (2019) Cascaded SMA-film based elastocaloric cooling. In: 2019 20th international conference solid-state sensors, actuators microsystems Eurosensors XXXIII (TRANSDUCERS EUROSENSORS XXXIII), 2019, pp 1467–1470. https://doi.org/10.1109/TRANSDUCERS.2019.8808605
62. Sharar DJ, Radice J, Warzoha R, Hanrahan B, Smith A (2021) Low-force elastocaloric refrigeration via bending. Appl Phys Lett 118:184103. https://doi.org/10.1063/5.0041500
63. Wang R, Fang S, Xiao Y, Gao E, Jiang N, Li Y, Mou L, Shen Y, Zhao W, Li S, Fonseca AF, Galvão DS, Chen M, He W, Yu K, Lu H, Wang X, Qian D, Aliev AE, Li N, Haines CS, Liu Z, Mu J, Wang Z, Yin S, Lima MD, An B, Zhou X, Liu Z, Baughman RH (2019) Torsional refrigeration by twisted, coiled, and supercoiled fibers. Science 366:216–221. https://doi.org/10.1126/science.aax6182
64. Wang R, Zhou X, Wang W, Liu Z (2021) Twist-based cooling of polyvinylidene difluoride for mechanothermochromic fibers. Chem Eng J 417:128060. https://doi.org/10.1016/j.cej.2020.128060
65. Qian S, Ling J, Hwang Y, Radermacher R, Takeuchi I (2015) Thermodynamics cycle analysis and numerical modeling of thermoelastic cooling systems. Int J Refrig 56:65–80. https://doi.org/10.1016/j.ijrefrig.2015.04.001
66. Cheng S, Xiao Y, Li X, Lin H, Hua P, Sheng L (2023) Buckling prevention of a single long NiTi tube compressive elastocaloric regenerator. Int J Solids Struct 271–272:112263. https://doi.org/10.1016/j.ijsolstr.2023.112263
67. Porenta L, Lavrenčič M, Dujc J, Brojan M, Tušek J, Brank B (2021) Modeling large deformations of thin-walled SMA structures by shell finite elements. Commun Nonlinear Sci Numer Simul 101:105897. https://doi.org/10.1016/j.cnsns.2021.105897
68. Watkins RT, Shaw JA (2018) Unbuckling of superelastic shape memory alloy columns. J Intell Mater Syst Struct 29:1360–1378. https://doi.org/10.1177/1045389X17733331
69. Tušek J, Engelbrecht K, Mikkelsen LP, Pryds N (2015) Elastocaloric effect of Ni-Ti wire for application in a cooling device. J Appl Phys 117:124901. https://doi.org/10.1063/1.4913878

70. Heggs PJ, Burns D (1988) Single-blow experimental prediction of heat transfer coefficients. Exp Therm Fluid Sci 1:243–251. https://doi.org/10.1016/0894-1777(88)90003-9
71. Šarlah A, Tušek J, Poredoš A (2012) Comparison of thermo-hydraulic properties of heat regenerators applicable to active magnetic refrigerators. Stroj Vestnik/J Mech Eng 58:16–22. https://doi.org/10.5545/sv-jme.2010.250
72. Trevizoli PV, Peixer GF, Nakashima AT, Capovilla MS, Lozano JA, Barbosa JR (2018) Influence of inlet flow maldistribution and carryover losses on the performance of thermal regenerators. Appl Therm Eng 133:472–482. https://doi.org/10.1016/j.applthermaleng.2018.01.055
73. Lei T, Navickaitė K, Engelbrecht K, Barcza A, Vieyra H, Nielsen KK, Bahl CRH (2018) Passive characterization and active testing of epoxy bonded regenerators for room temperature magnetic refrigeration. Appl Therm Eng 128:10–19. https://doi.org/10.1016/j.applthermaleng.2017.08.152
74. Nickolay M, Martin H (2002) Improved approximation for the Nusselt number for hydrodynamically developed laminar flow between parallel plates. Int J Heat Mass Transf 45:3263–3266. https://doi.org/10.1016/S0017-9310(02)00028-5
75. Kaviany M (1991) Principles of heat transfer in porous media. Springer, New York. https://doi.org/10.1007/978-1-4684-0412-8
76. Shah RK, Sekulić DP (2003) Fundamentals of heat exchanger design. Wiley, New Jersey
77. Zhang J, Zhu Y, Yao S, Sun Q (2023) Highly efficient grooved NiTi tube refrigerants for compressive elastocaloric cooling. Appl Therm Eng 228:120439. https://doi.org/10.1016/j.applthermaleng.2023.120439